Journal of Catalysis **208,** 467–478 (2002)
doi:10.1006/jcat.2002.3609

Alumina- and Alumina–Zirconia-Supported PtSn Bimetallics: Microstructure and Performance for the *n*-Butane ODH Reaction

C. Larese,* J. M. Campos-Martin,* J. J. Calvino,† G. Blanco,† J. L. G. Fierro,*,[1] and Z. C. Kang‡

*Instituto de Catálisis y Petroleoquímica, CSIC, Cantoblanco, 28049 Madrid, Spain; †Departamento de Ciencia de los Materiales e Ingeniería Metalúrgica y Química Inorgánica, Facultad de Ciencias, Universidad de Cádiz, Apartado 40, 11510 Puerto Real (Cádiz), Spain; and ‡Department of Chemistry and Biochemistry, Arizona State University, Tempe, Arizona 85287-1604

Received January 8, 2002; revised March 14, 2002; accepted March 16, 2002

In the present work, a number of Al_2O_3- and Al_2O_3–ZrO_2-supported catalysts were prepared and studied. The microstructure of the particles formed in these systems was analyzed by high-resolution electron microscopy (HREM). HREM images of Al_2O_3-supported catalysts revealed a broad particle-size distribution, with a major Pt phase exhibiting diameters in the range 5–15 nm with a shell of $PtSn_4$. Also, $PtSn_4$ and very large particles were detected. In the case of Al_2O_3–ZrO_2-supported catalysts, ZrO_2 was present as nanometer-size crystals of the tetrahedral and monoclinic phases and the trimodal distribution of metal particles disappeared, the smaller particles being dominant. Photoelectron spectroscopy showed that in used catalysts tin is oxidized while platinum remains partially reduced. Upon activation (reduction at 623 or oxidation at 773 K/reduction at 873 K), tin became partially reduced; however, no significant changes were seen in the oxidation state of platinum. The catalysts were tested in the oxidative dehydrogenation of *n*-butane. The major reaction products were carbon oxides and olefins, with much smaller amounts of cracking and isomerization products. The incorporation of tin into the Pt/Al_2O_3 catalyst led not only to an increase in conversion but also to an inhibition of cracking reactions. Deactivation was observed in all cases. Surface analysis by photoelectron spectroscopy of exhausted catalysts revealed the formation of carbonaceous deposits on the catalyst surface, indicating that coking is responsible for catalyst deactivation.

Key Words: **platinum–tin catalysts; alumina–zirconia; *n*-butane oxidative dehydrogenation; HREM and XPS analyses.**

INTRODUCTION

The abundance and low cost of low-molecular-weight paraffins has generated much interest in their oxidative transformation to olefins. Oxidative dehydrogenation (ODH) represents an attractive economic option that would bypass the common energy-intensive endothermic steam cracking or dehydrogenation processes currently employed to produce olefins and intermediates from gas liquefied products (GLP) and petroleum feedstocks (1–3).

Alumina-supported platinum catalysts have long been used for the dehydrogenation of C_4 paraffins (4–9). However, the reaction conditions imposed by thermodynamics that are required to perform the dehydrogenation reaction are so stringent that they result in catalyst deactivation. Under typical reaction conditions, Pt/Al_2O_3 catalysts exhibit good activity but the yield to butenes (and butadiene) is low because the platinum particles also lead to side C–C hydrogenolysis reactions, with the subsequent formation of C_1–C_3 products and coke deposits. They must be thus regenerated at rather short intervals. A significant advance was achieved in the 1970s with the introduction of PtRe bimetallics able to operate for much longer onstream periods. A major drawback of RePt-reforming catalysts, however, is that they must be activated in a tedious process that usually involves S-poisoning during a break-in period. Currently, since reformers are well equipped with devices to ensure continuous catalyst regeneration, other bimetallic catalysts that operate on simple activation procedures are being used. Among these, the PtSn bimetallic catalyst remains prominent (1, 10, 11).

The incorporation of tin into base Pt/Al_2O_3 catalysts has a positive effect on the selectivity to olefins, but at the expense of the hydrogenolysis reactions. The reasons for this behavior are not fully understood even after 30 years of intense efforts. It has been widely documented that the state of metals depends on the properties of the support (11, 12), the preparation method (13, 14), the metal precursor used (15–17), the degree of metal loading (18), and the pretreatment conditions of the samples (1, 19). All these factors determine the nature of the active metals and hence the final catalytic behavior. It has been proposed that the observed superior catalytic performance may be the result of a higher dispersion of platinum and platinum crystallite stabilization by Sn (20, 23). Other authors have suggested that Sn weakens the interaction energy between coke and the Pt surface (24); the carbonaceous fragments are more mobile and are thus able to migrate toward the support surface. Many of the explanations advanced are based on the formation of bimetallic PtSn, which exhibits better performance than Pt alone (19).

[1] To whom correspondence should be addressed. Fax: +34 91 585 4760. E-mail: jlgfierro@icp.csic.es.

0021-9517/02 $35.00

Recently, combining transmission electron microscopy (TEM), X-ray dispersive energy analysis (EDX), and X-ray diffraction (XRD), several works have been undertaken with the aim of identifying possible PtSn intermetallic compounds in platinum–tin dehydrogenation catalysts. Thus, Llorca *et al.* (15, 19) studied $PtSn/SiO_2$ and $PtSn/Al_2O_3$ catalysts prepared from the *cis*-$[PtCl(SnCl_3)(PPh_3)_2]$ complex and found that upon H_2-reduction at 473 and 873 K for 16 h, the only phase present was the PtSn alloy (15, 19). Similarly, a PtSn phase was also observed in PtSn/MgO catalysts (12). On the other hand, Srinivasan *et al.* (20) provided experimental evidence for the existence of two intermetallic phases, PtSn and $PtSn_2$, in Al_2O_3-supported catalysts. These catalysts were prepared by the coimpregnation of H_2 $PtCl_6$ and $SnCl_4$ and then reduced at 773 K for 18 h. Huang *et al.* (18) investigated the presence of PtSn alloy in catalysts supported on alumina, prepared by six different impregnation methods and with platinum loadings in the range 0.3–3.0 wt% while maintaining a Sn/Pt ratio of 1. After testing in the reforming reaction of octane, they observed the presence of a major PtSn alloy, together with minor amounts of other PtSn bimetallic phases.

Due to the evident complexity and sensitivity of these systems to a high number of variables, our aim here was to investigate the microstructure and the surface properties associated with this structure in $PtSn/Al_2O_3$ and $PtSn/ZrO_2$–Al_2O_3 catalysts. To gain a better understanding of the properties that contribute to their effectiveness, the surface characteristics of these PtSn catalysts were approached using HREM (high-resolution electron microscopy), X-ray photoelectron spectroscopy (XPS), and hydrogen chemisorption techniques. The importance of this surface microstructure was then examined in relation to the performance for the oxidative dehydrogenation (ODH) reaction of *n*-butane.

EXPERIMENTAL

Catalyst Preparation

The catalysts were prepared by the incipient wetness impregnation technique. The supports were γ-Al_2O_3 (Girdler Sud Chemie; S_{BET}, 188 m^2/g; mesopore size, 8.5 nm) calcined in air at 1173 K for 8 h and two ZrO_2–Al_2O_3 supports with 9 and 13 wt% ZrO_2 and S_{BET} of 99 and 86 m^2/g, respectively. These ZrO_2–Al_2O_3 mixed supports were prepared by controlled hydrolysis of a zirconium alkoxide, following a previously described methodology (21). For the sake of simplicity, these supports were labeled A, 9ZA, and 13ZA, respectively. Some textural and surface characterizations of these supports have been reported previously (21). Bimetallic catalysts were prepared from a water solution of the metallic precursors H_2PtCl_6 and $SnCl_2 \cdot 2H_2O$ by coimpregnation. Platinum loading was 2 wt% in all the cases and tin loading was 1.2 wt%, corresponding to a Sn/Pt atomic ratio of 1. In addition, monometallic Pt/A and Pt/9ZA catalysts, containing 2 wt% Pt, were also prepared according to the same methodology. Impregnates were dried at 383 K. The bimetallic catalysts were labeled PtSn/A, PtSn/9ZA, and PtSn/13ZA.

Catalyst Characterization

Hydrogen chemisorption measurements were carried out volumetrically in a high vacuum line and gas-handling system. This apparatus is equipped with a capacitance MKS Baratron pressure transducer, model 270 B. Hydrogen adsorption isotherms were obtained at ambient temperature (298 K) up to a final equilibrium pressure of 100 mbar. Prior to chemisorption experiments, the samples were either calcined *in situ*, by heating in air at a rate of 10 K/min up to 773 K followed by reduction in hydrogen at 773 K for 15 min, or only reduced in hydrogen at 773 K for 15 min.

High-resolution electron microscopy (HREM) was performed on two microscopes, a JEOL 2000EX (200 KeV accelerating voltage, Cs = 0.7 mm) with a 0.21-nm structural resolution, and a JEOL 4000EX (400 KeV accelerating voltage, Cs = 1 mm). The resolution achievable in the latter device extends further, up to 0.19 nm. HREM images were recorded, at 400–600 K nominal magnification, on KODAK SO-163 photographic plates, which were developed using conventional procedures. At least 50 plates corresponding to different positions were recorded for each sample so that statistically significant conclusions could be obtained. For their quantification and analysis, selected regions of these micrographs were digitized using a COHU-4910 CCD camera. Image acquisition and analysis were carried out using different routines developed at the University of Cádiz and coded in SEMPER6+ software from Synoptics. The diffractograms, or digital diffraction patterns (DDPs), reported in this work correspond to the log-scaled power spectrum of the Fourier transform of the bidimensional intensity distribution in the digitized images. For observation under the electron microscopes, the catalysts were reduced in a 5% H_2/Ar flow at 623 K or calcined in air at 773 K and subjected to further reduction in 5% H_2/Ar at 873 K. To prevent the fast and uncontrolled reoxidation of the reduced catalysts during their transfer to the electron microscope chamber, the last step of the preparation of all the samples was a passivation treatment, performed as follows: the samples were cooled to 191 K (solid–liquid acetone trap) in a flow of He; then the gas flow was switched to 5% O_2/He. After a half an hour treatment with this oxidizing mixture at 191 K, they were slowly warmed to 298 K. For their observation in the electron microscope, the catalyst powders were dispersed on holey carbon-coated Cu grids.

Photoelectron spectra (XPS) were recorded using a Escalab 200R spectrometer equipped with a hemispherical analyzer, operating in a constant pass energy (20 eV) mode, and Mg $K\alpha$ X-ray radiation source ($h\nu = 1253.6$ eV). Prior

to analysis, the samples used were reduced in the pretreatment chamber of the spectrometer at 573 K for 1 h. After these treatments, samples were outgassed until 10^{-6} mbar and were then placed in the analysis chamber. A base pressure of 2×10^{-9} mbar was maintained during data acquisition. The spectral regions of C 1s, Al 2p, Zr 3d (if present), Sn 3d, and Pt $4d_{5/2}$ photoelectrons were recorded under high-resolution conditions and averaged for a number of scans in order to obtain good signal-to-noise ratios. Once the background had been removed, the spectra thus obtained were fitted to Lorentzian and Gaussian lines to obtain the number of components, peak positions, and areas. The Al 2p line at 74.5 eV was used as an internal standard. The surface Sn/Al, Pt/Al, and C/Pt atomic ratios were estimated from the integrated intensities of Sn $3d_{5/2}$, Pt $4d_{5/2}$, C 1s, and Al 2p lines corrected by atomic sensitivity factors (22).

Activity Measurements

Catalytic experiments aimed at exploring the oxidative dehydrogenation of *n*-butane were performed at atmospheric pressure in a continuous flow system. The reactor was made of quartz with an inner diameter of 0.4 cm. Samples consisting of 0.200 g of each catalyst were diluted with SiC up to 1 cm^3 and further loaded into the reactor, supported on both sides by quartz wool. Total flow was 73.5 ml/min, with an *n*-butane molar concentration of 20.4% and *n*-butane/oxygen ratio equal to 1. Nitrogen was used as diluting agent. Before the reactions, samples were reduced *in situ* in a 10% H_2/N_2 flow at 623 K for 15 min or calcined in air at 773 K for 15 min, followed by further reduction in 10% H_2/N_2 at 873 K for 15 min. The reaction temperatures explored spanned the 573- to 773-K range. Exit gases were analyzed with a GC Hewlett Packard (HP 6890) fitted with TCD and FID detectors and a Porapack Q, a molecular sieve, and HP-Plot Al_2O_3 columns.

RESULTS

Catalyst Characterization

The hydrogen chemisorption data for monometallic (Pt) and bimetallic (PtSn) samples are summarized in Table 1. Two sets of H_2-adsorption experiments were conducted on each sample: reduction in hydrogen at 773 K, and air calcination at 773 K, followed by H_2 reduction at the same temperature. For bimetallic catalysts supported in alumina, the H/Pt ratio was very low in comparison with that found for the monometallic catalysts. This was observed independently of how the treatment was carried out and may be related to the presence of particles of considerable size, strong interactions between metals, or a combination of both phenomena. Although in the bimetallic catalysts supported on ZA the H/Pt ratio was lower than for the monometallic catalysts, the differences were less marked than in alumina catalysts. This suggests that the incorporation of zirconia to the support would modify the microstructure of the catalysts and the interaction between metals in different ways in comparison with the situation obtained with alumina.

TABLE 1

Hydrogen Volumetric Adsorption for Mono- and Bimetallic Catalysts at 298 K

Catalyst	Treatment	Atoms H/g cat.	H/Pt
Pt/A	Redn. 773 K	1.37×10^{19}	0.63
	Air 773 K, redn. 773 K	3.53×10^{18}	0.16
PtSn/A	Redn. 773 K	1.81×10^{18}	0.09
	Air 773 K, redn. 773 K	9.29×10^{17}	0.05
Pt/9ZA	Redn. 773 K	8.15×10^{18}	0.35
	Air 773 K, redn. 773 K	1.29×10^{19}	0.56
PtSn/9ZA	Redn. 773 K	5.7×10^{18}	0.26
	Air 773 K, redn. 773 K	6.5×10^{18}	0.29

High-Resolution Electronic Microscopy (HREM)

PtSn/A catalysts. HREM study of the samples supported on alumina aimed at gaining insight into the state of the metallic components after a given pretreatment. Two pretreatments were selected: (i) reduction in a 5% H_2/Ar flow at 623 K; and (ii) air calcination at 773 K and further reduction in 5% H_2/Ar at 873 K. The size distribution of the metallic aggregates was one of the key aspects investigated. The HREM images obtained from the PtSn/A sample subjected to pretreatments (i) and (ii) pointed to the presence of supported particles in three different size ranges. Thus, as shown in Fig. 1, there was a fraction of small particles with diameters ranging between 1 and 2 nm. This type of particle is comparatively much more abundant in the catalyst after pretreatment (ii) than in the catalyst directly reduced at

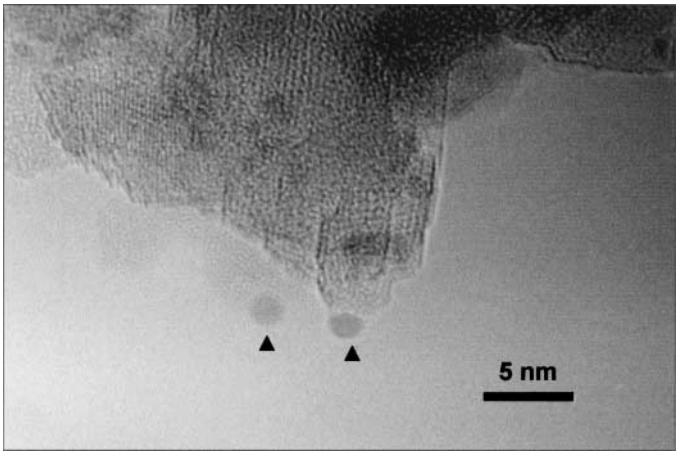

FIG. 1. HREM views of the PtSn/A catalyst oxidized at 773 K and further reduced at 873 K. Note the presence of very small particles (marked with arrows).

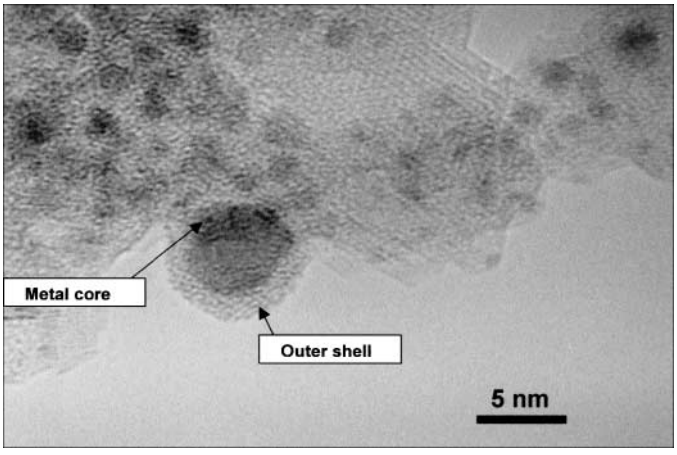

FIG. 2. HREM image of the PtSn/A catalyst oxidized at 773 K and further reduced at 873 K. Note the presence of the core-shell structure on the larger particles.

623 K. The rapid fluctuation of these small particles under the electron beam erases the lattice fringe contrast in the HREM images, precluding any assignment to a particular metallic phase. In any case, one feature that did seem to be clear is that these small particles are clean; i.e., they are not covered by a thin layer of other kinds of atoms.

A second type of particle present in the PtSn/A samples after pretreatments (i) and (ii) were those exhibiting diameters in the 5- to 15-nm range (Fig. 2). Most of the particles in this class presented a shell-core structure. It was clear that a crystalline layer, with a thickness of about 1 nm, was covering the surface of these nanometer-size particles. Phase assignment of such tiny layers from HREM contrasts is a difficult task, not only because of the rather large number of possibilities that must be considered in the analysis—among which pure Pt or Sn and up to at least five different PtSn alloys of varying stoichiometries should be considered—but also because of the reduced width of the areas involved. Nevertheless, after analyzing the images of a large number of these particles, two results emerged as meaningful. First, in the digital diffraction patterns (DDPs) obtained from some of these layers, a 0.569-nm lattice spacing was identified (Fig. 3a). Such d-spacing is not present either in Pt or Sn. As judged from this d-spacing, the Al_2O_3 substrate can be precluded. However, the $PtSn_4$(002) planes could be responsible for this diffraction spot. This suggests that these particles would present a tin-rich outer surface. Second, on looking at the core, careful analysis of the DDPs indicated that they were most likely constituted by a Pt-rich phase. Figure 3b shows one of these coated particles. The image was recorded at a defocus value, which enhanced the contrast due to the core. In the corresponding DDP (inset in Fig. 3b), the 0.227-nm spots characteristic of Pt(111) planes can be seen. Likewise, the HREM images of some particles in the medium-size range, such as that shown in Fig. 4, could be unambiguously assigned to Pt, taking into account the bidimensionally resolved contrast. In this particular case, the DDP of the particle contains the reflections characteristic of Pt in [110] orientation.

Only in a very limited number of cases, which cannot in fact be considered as representative, were particles in this size range found to exhibit contrasts that could be assigned to a bulk platinum–tin alloy phase. Figure 5 shows one of these particular cases. Note in Fig. 5 the dramatic change in the geometry of the image contrasts with respect to those shown by the particles in previous figures. Phase analysis indicated that this particular image can be assigned to a $PtSn_4$ alloy particle. This result is in good agreement with those commented previously.

Finally, a third type of particle was found in these samples (Fig. 6). Specifically, quite large and dense particles with size in the tens of nanometers range (60–100 nm) were observed. These particles are extremely large to allow a

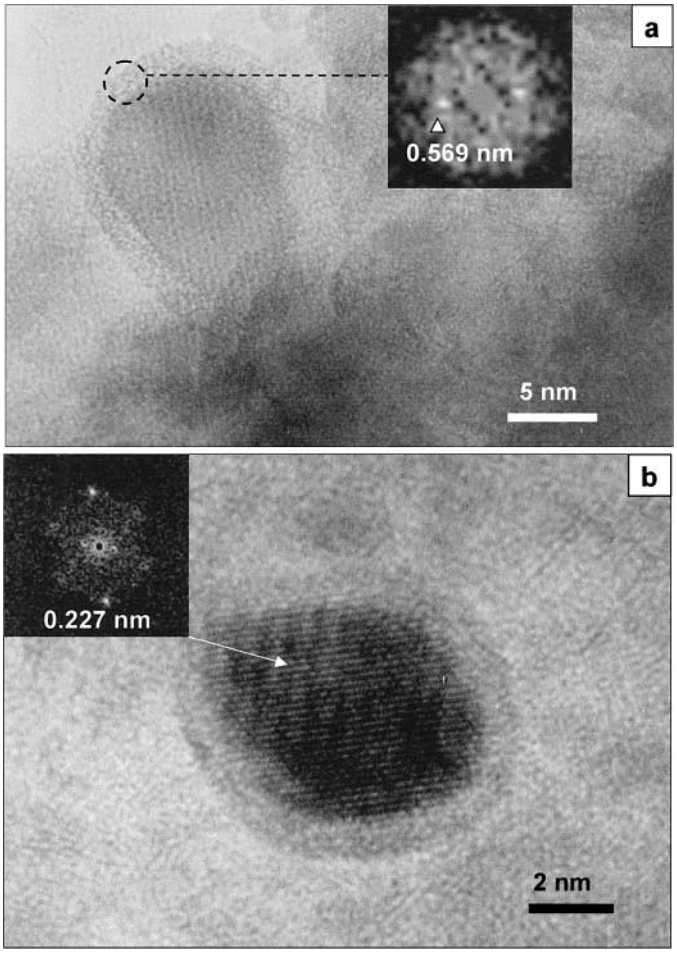

FIG. 3. (a) HREM detail of the PtSn/A catalyst oxidized at 773 K and further reduced at 873 K. The DDP inset corresponds to the encircled area of the particle outer shell. Spots at 0.569 nm are present. (b) HREM image of the same catalyst. The DDP inset was calculated from the core zone of the particle. Spots at 0.227 nm can be assigned to metallic Pt.

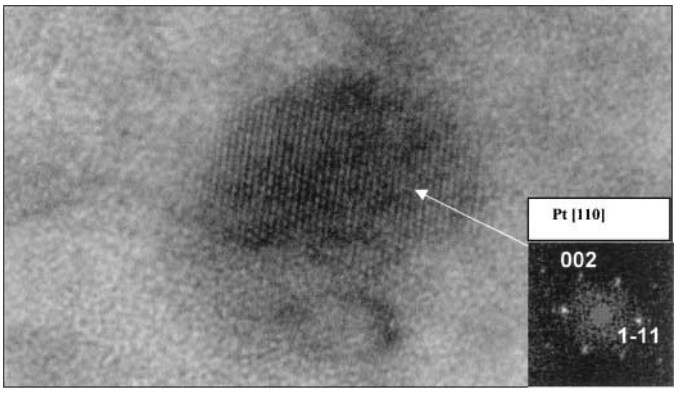

FIG. 4. HREM detail of the PtSn/A catalyst oxidized at 773 K and further reduced at 873 K. The DDP inset corresponds to the particle. It can be assigned to [110] metallic Pt.

significant transmission of the electron beam. Consequently they appear as black spots in the HREM images, from which no structural information can be retrieved. Such contrasts must be due to metal particles, either pure or alloyed. This latter type of particles was particularly abundant in samples reduced at 623 K and this may correlate with the low number of very small metal particles observed in this sample. The incorporation of metal atoms to the large particle fraction should, in fact, have a dramatic effect on the number of highly dispersed particles.

PtSn/13ZA samples. The HREM work on PtSn/13ZA samples addressed two aspects: (i) the state of the metallic components; and (ii) the characterization of the zirconia phases of the substrate. With respect to point (i), the same types of features were analyzed, i.e., the particle size, the chemical nature, and the surface structure of the particles. Regarding point (ii), both the dispersion of ZrO_2 phases on the major Al_2O_3 component of the mixed ZA

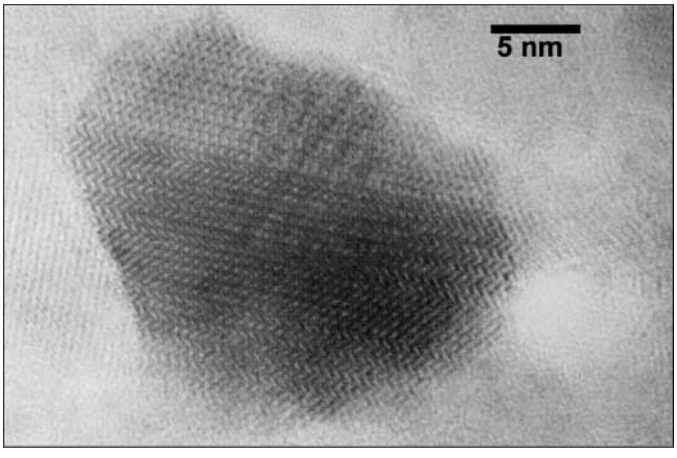

FIG. 5. HREM detail of the PtSn/A catalyst oxidized at 773 K and further reduced at 873 K. Contrasts in the image can be assigned to a $PtSn_4$ intermetallic phase.

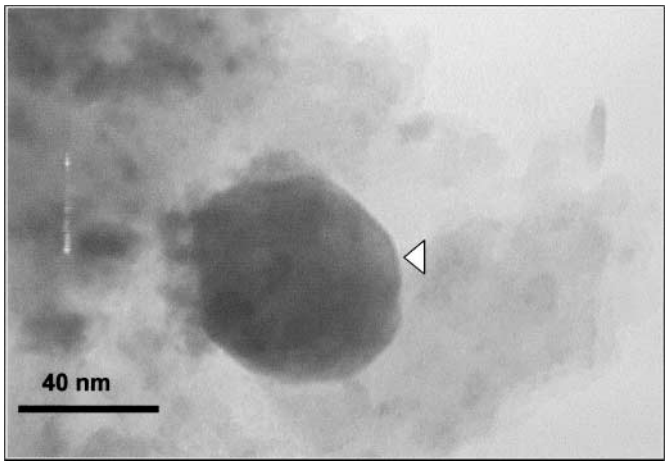

FIG. 6. Low magnification views of the PtSn/A catalyst reduced at 623 K. Note the presence of huge metal particles, with diameters close to 100 nm (marked with arrows).

support and the crystallographic nature of the zirconia were studied.

The first point of note is that in both samples—reduced at 623 K or calcined at 773 K and subjected to further reduction at 873 K—zirconia was present as nanometer-size crystalline particles (Fig. 7), with diameters in the 2- to 10-nm range. From this observation it may be inferred that zirconia is highly dispersed in both catalysts. This further complicates the analysis of the HREM images. In this case, it becomes absolutely necessary, given the small size of the zirconia particles, to rely on bidimensionally resolved zone axis images to distinguish and identify the metal phases. In fact, one micrograph contains a huge number of

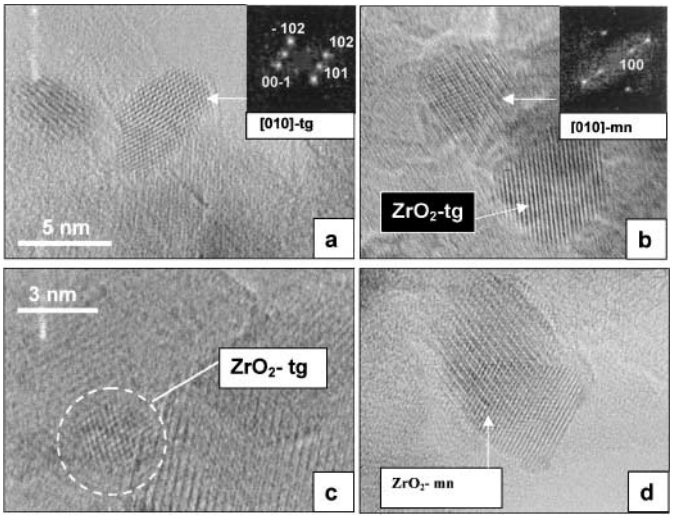

FIG. 7. HREM images of the PtSn/13ZA catalyst: (a,b) reduced at 623 K; (c,d) oxidized at 773 K and further reduced at 873 K. Nanometer-size tetragonal (tg) and monoclinic (mn) zirconia crystallites are seen.

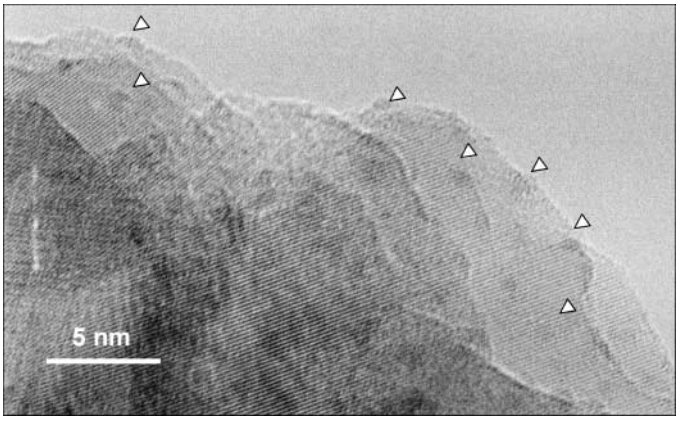

FIG. 8. HREM images of the oxidized and reduced PtSn/13ZA catalyst showing small Pt particles (some marked with arrows).

nanometer-size crystals, in many cases superimposed over each other. Fourier analysis of the contrasts of the zirconia particles indicates the presence in both samples of tetragonal and monoclinic polymorphs. Thus, characteristic [010]-tetragonal and [010]-monoclinic zirconia images were recorded (Figs. 7a,c and 7b,d, respectively).

With respect to the metal phase, in the sample subjected to pretreatment (ii), the most important aspect to be stressed is the presence of a large number of very small Pt particles, in most cases smaller than 1 nm (Fig. 8). These particles were clearly identified from bidimensional lattice images in the [110] (Fig. 9a) and [001] (Fig. 9b) orientations. None of these particles could be detected in the sample directly reduced at 623 K (pretreatment (i)). Only the image of one particle in sample calcined and reduced showed contrasts characteristic of the $PtSn_4$ alloy phase. Moreover, only in a very limited number of cases were particles, whose contrasts could be assigned to Sn, found.

In a comparison with PtSn/A samples, the most relevant difference was the disappearance of the trimodal distribution of metal particles in the Zr-containing samples. Thus, in the PtSn/13ZA samples, particles in the medium and very large size ranges were not significant at all. This suggests a more homogeneous distribution and higher dispersion of the metallic components in these catalysts. Such a distribution would have great impact on catalytic performance.

Catalytic Activity

Influence of pretreatment. The catalytic activity of the PtSn/A and PtSn/9ZA catalysts in the oxidative dehydrogenation of *n*-butane after pretreatments (i), reduction in a 10% H_2/N_2 flow at 623 K for 15 min, and (ii), calcination in air at 773 K for 15 min and further reduction in 10% H_2/N_2 flow at 873 K for 15 min, is shown in Fig. 10. For all the catalysts tested, the main reaction products were CO_2, C_4 olefins (*trans*-2-butene, 1-butene, *cis*-2-butene, and 1,3-butadiene), and H_2O. Oxygen was completely consumed immediately after the start of the reaction. The reaction profiles were similar for all the catalysts, although *n*-butane conversion was strongly dependent on the catalyst pretreatment. The calcined-reduced catalysts (pretreatment (ii)) achieved higher conversion values than did their reduced counterparts. Product distribution was also strongly dependent on the pretreatment employed. Thus, the isomerization reaction was minimized to 0.5% in the catalyst subjected to pretreatment (ii), whereas pretreatment (i) led to a much higher amount of isomerization products (up to 10%). These different types of behavior of the catalysts in the ODH reaction could be related to their microstructure. Since the catalysts subjected to pretreatment (i) exhibited a particle-size distribution shifted toward higher sizes with respect to that of their counterparts after pretreatment (ii), as revealed by HREM experiments, it is possible to infer a relationship between isomerization selectivity and the large size of the metal particles. Taking into account the fact that the catalyst subjected to pretreatment (ii) exhibited better performance in the ODH reaction, this pretreatment was selected for ensuing activity experiments.

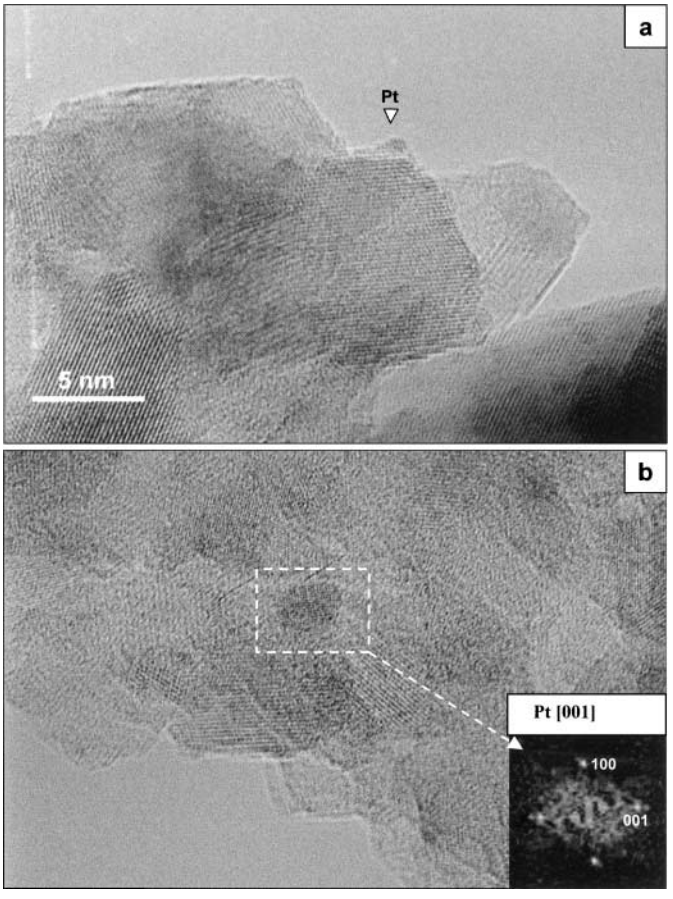

FIG. 9. HREM images of the PtSn/13ZA catalyst oxidized at 773 K and further reduced at 873 K. (a) A small Pt cluster in [110] orientation can be observed; (b) a Pt particle down the [001] zone axis has been imaged.

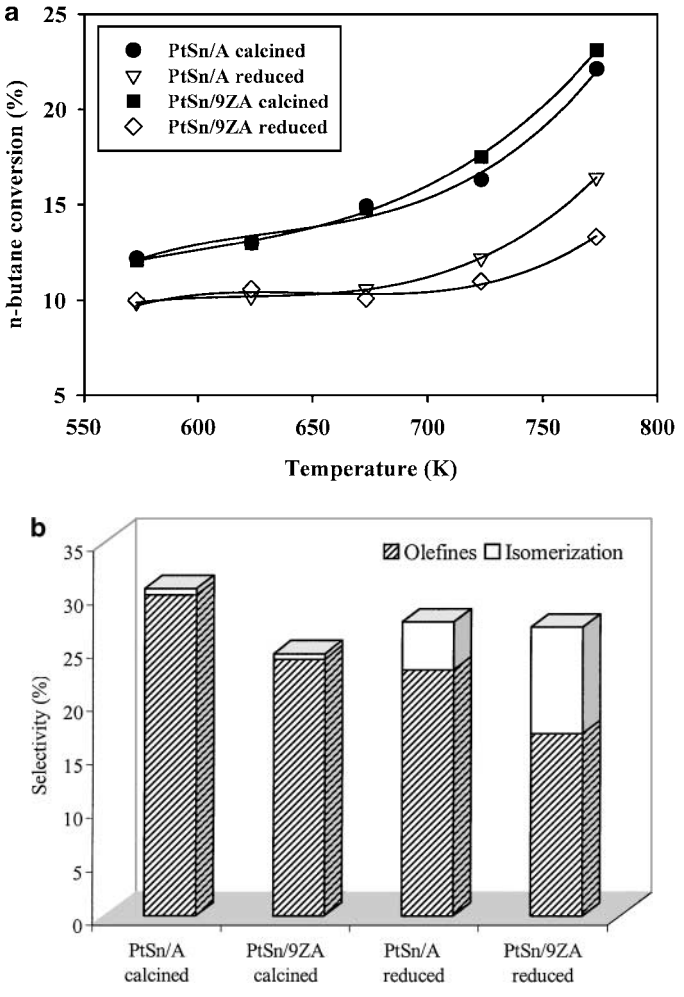

FIG. 10. *n*-Butane conversion and selectivity (at 15% conversion) as a function of the reaction temperature for calcined–reduced and reduced PtSn/A and PtSn/9ZA catalysts.

Influence of tin addition. The catalytic behaviors of the PtSn/A, PtSn/9ZA, Pt/A, and Pt/9ZA catalysts are shown in Fig. 11. Comparison of the Sn-free and PtSn catalysts revealed that tin incorporation produces an increase in *n*-butane conversion. In addition, an increase in selectivity to olefins was observed in the PtSn/A and PtSn/9ZA catalysts in comparison with the Pt/A and Pt/9ZA types, respectively. However, this effect was much more pronounced in the zirconia-free samples than with the Pt/9ZA and PtSn/9ZA samples. By contrast, the presence of tin almost suppressed the isomerization reaction, as indicated by the lower degree of isomerization (below 1%) in the PtSn/A and PtSn/9ZA catalysts.

Stability Tests

Stability tests were conducted at 723 K on the monometallic Pt/A and the bimetallic PtSn/A, PtSn/9ZA, and PtSn/13ZA catalysts. The values of *n*-butane conversion and selectivity to cracking and isomerization products, after 1000 min of reaction, are summarized in Table 2. As cracking products, methane, ethane, propane, ethylene, and propylene were found, whereas those of isomerization were isobutane and isobutylene. The C_4 olefin distributions for each catalyst are also shown in Table 2. The conversion and selectivity profiles versus the reaction time for all the catalysts are shown in Fig. 12. Loss of activity with the reaction time, faster at shorter times and much slower at longer times, was observed for all the catalysts. This decrease, around 40%, was similar for all the bimetallic catalysts, whereas it became more pronounced in the monometallic catalysts (Pt/A). The origin of this deactivation must lie in the formation of coke deposits on the catalyst surface. It should be stressed that under the experimental conditions employed in the present work oxygen conversion was complete. Therefore, deactivation by coke cannot be ruled out.

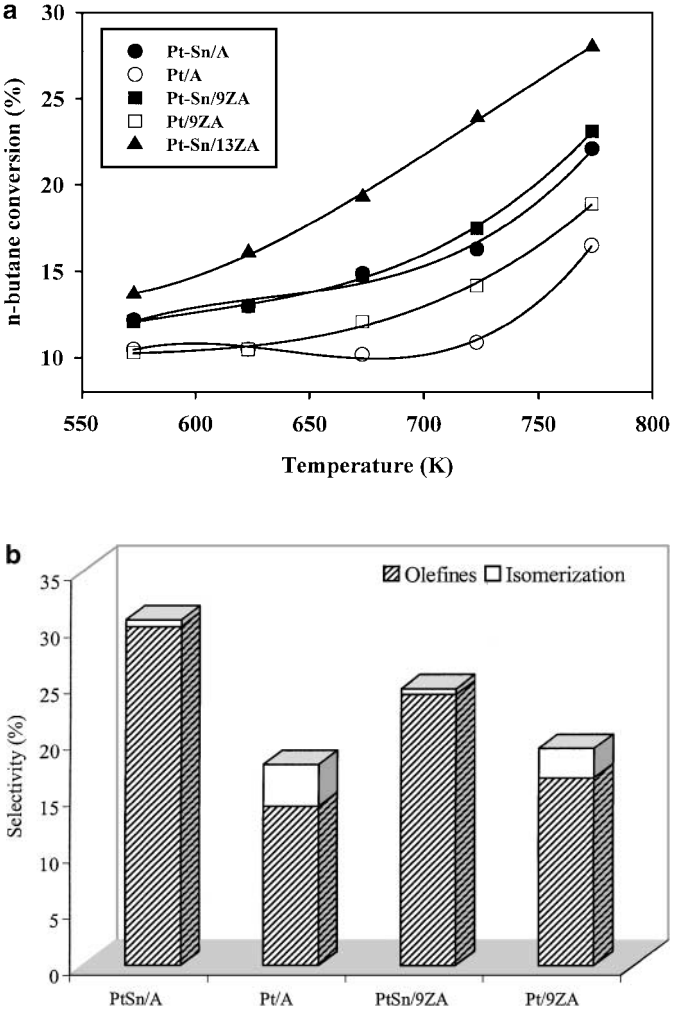

FIG. 11. *n*-Butane conversion and selectivity (at 15% conversion) as a function of the reaction temperature for calcined–reduced mono- and bimetallic catalysts.

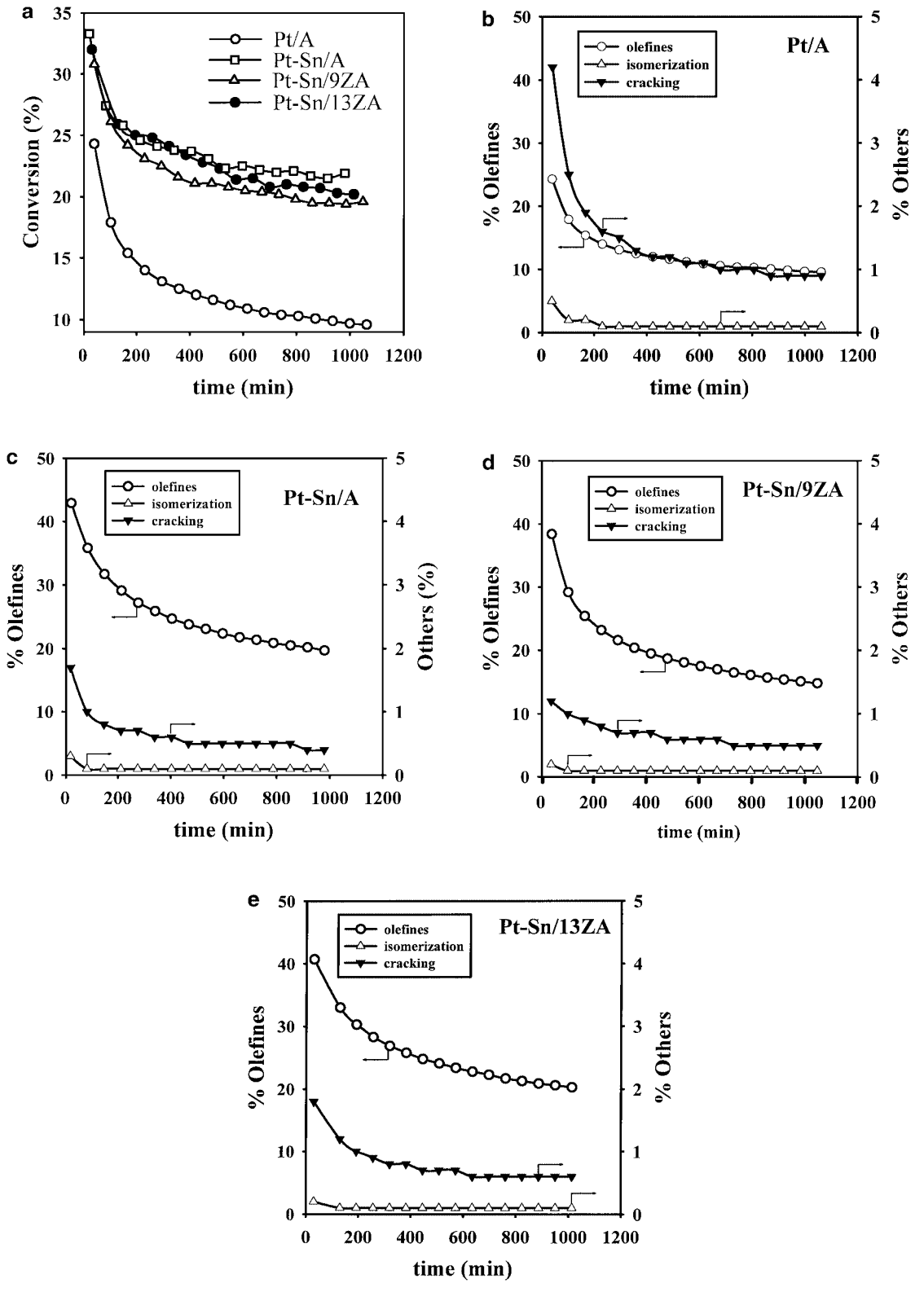

FIG. 12. Comparison of the catalytic behavior in the *n*-butane ODH reaction at 723 K for calcined–reduced mono- and bimetallic catalysts.

TABLE 2

Conversion and Selectivity Data for the Catalytic Oxidative Dehydrogenation of *n*-Butane at 723 K after 1000 min on Stream[a]

	X *n*-butane (%)		Selectivity (%)			Olefin distribution (%)			
Catalyst	Initial	1000 min	CR	ISO	DEH	*trans*-2-Butene	1-Butene	*cis*-2-Butene	1,3-Butadiene
Pt/A	24.3	9.6	0.9	0.1	9.6	35.2	30.6	27.2	7.1
PtSn/A	33.3	21.9	0.4	0.1	19.7	35.8	27.4	25.6	11.2
PtSn/9ZA	30.8	19.6	0.5	0.1	14.8	32.4	27.5	23.4	16.8
PtSn/13ZA	32.0	20.2	0.6	0.1	20.3	34.2	27.4	24.4	14.1

[a] CR, cracking selectivity; ISO, isomerization selectivity; DEH, dehydrogenation selectivity.

The selectivity to dehydrogenation products was low, obtaining around 80% of carbon oxides. A slightly higher selectivity to olefins was observed for the PtSn/13ZA catalyst. Regarding selectivity to isomerization products, this was similar for all the catalysts, with values of about 0.1%. On comparing bimetallic and monometallic catalysts, it was possible to observe that the presence of tin caused a decrease in the cracking product selectivity (methane, ethane, propane, ethylene, and propylene), probably because the PtSn interaction decreases the hydrogenolytic capacity of platinum. When tin was added, 1,3-butadiene formation was increased from 7 to 11%, (see catalysts Pt/A versus PtSn/A in Table 2). Later, the addition of ZrO_2 elicited a further increase in the proportion in 1,3-butadiene, with values of 14–16% being obtained. This increase took place at the expense of a decrease in secondary olefins (2-butenes).

Surface Analysis of the Catalysts Used

Surface analysis of used catalysts in the ODH reaction provided information about the chemical state of Pt and Sn and also about the surface exposure of the metals at the catalyst surface. The Pt 4d, Sn 3d, and C 1s spectra were recorded for the used catalysts in the ODH reaction and also for the same catalysts after *in situ* regeneration in the pretreatment chamber of the spectrometer, using air at 773 K for 1 h followed by H_2 treatment at 773 K for 15 min.

Table 3 gives the position of the main photoelectron peaks for the PtSn/A and PtSn/13ZA samples after referencing them to the Al 2p binding energy of 74.5 eV. For the sake of comparison, the Pt $4d_{5/2}$ and Sn 3d core levels of PtSn/A are depicted in Fig. 13, and the corresponding spectra for the PtSn/13ZA samples are shown in Fig. 14. On applying peak fitting procedures, the Sn $3d_{5/2}$ peaks for all the samples were satisfactorily fitted to two components. For the PtSn/A sample used, the Sn $3d_{5/2}$ peak shows a minor component at 486.9 eV and a major one at 487.9 eV, and these almost coincide for the used PtSn/13ZA counterpart. However, after the regeneration procedure, consisting of oxidation at 773 K followed by H_2 reduction at 773 K, this resulted in a shift of the two components to lower binding energies. Thus, the Sn $3d_{5/2}$ components for the PtSn/A subjected to the regeneration cycle appeared at 485.5 and 487.5 eV and, simultaneously, the intensity of the former peak increased with respect to its used counterpart. Similar findings were seen for the Sn $3d_{5/2}$ peak profile for the regenerated PtSn/13ZA sample.

TABLE 3

XPS Data for Pt–Sn Bimetallic Catalysts after ODH Reaction and Regeneration Treatment

Catalyst	Treatment	Pt 4d	Sn $3d_{5/2}$	Sn/Al	Pt/Al	Pt/C
PtSn/A	Air 773 K	314.9	487.6	0.036	0.0021	—
	H_2 773	316.1	486.2			
	After ODH	314.5	487.9	0.011	0.0011	0.0060
	reaction	316.2	486.9			
	Regeneration	314.3	487.5	0.012	0.0012	0.0210
	Air/H_2 773 K	316.2	485.5			
PtSn/13ZA	Air 773 K	314.1	487.2	0.14	0.0074	—
	H_2 773 K	315.2	485.4			
		316.1				
	After ODH	314.6	487.8	0.018	0.0010	0.0018
	reaction	315.8	486.8			
		317.2				
	Regeneration	314.4	486.9	0.020	0.0013	0.0210
	Air/H_2 773 K	316.1	485.3			

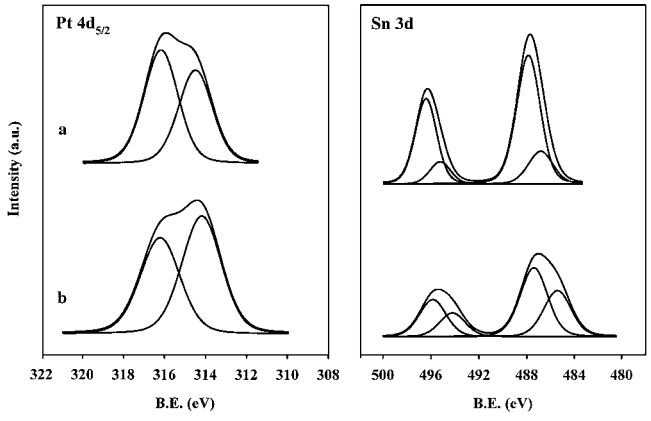

FIG. 13. Pt $4d_{5/2}$ and Sn 3d core-level spectra of PtSn/A catalysts: (a) after the *n*-butane ODH reaction; and (b) after regeneration pretreatment.

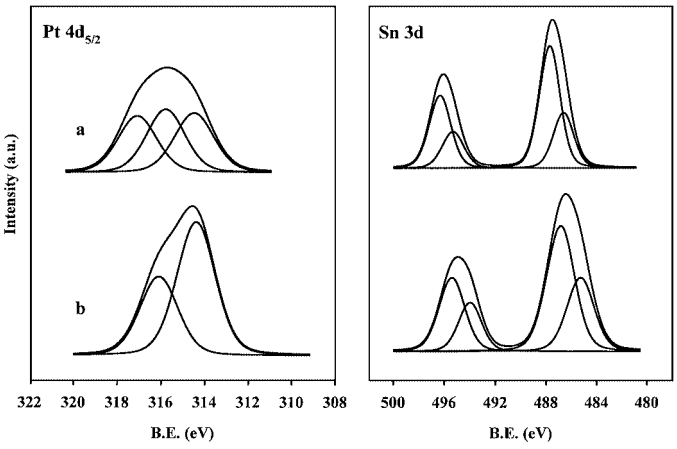

FIG. 14. Pt $4d_{5/2}$ and Sn 3d core-level spectra of PtSn/13ZA catalysts: (a) after the *n*-butane ODH reaction; and (b) after regeneration pretreatment.

The Pt $4d_{5/2}$ profile of the used PtSn/A sample shows two components, at 314.5 and 316.2 eV, the latter being slightly more intense than the former. For the PtSn/13ZA sample, the Pt $4d_{5/2}$ profile was more complex: the components at 314.6 and 315.8 eV were accompanied by a third one, at 317.2 eV. In the PtSn/A catalyst subjected to the oxidation–reduction cycle, the Pt $4d_{5/2}$ profile exhibited the same two components as in the used counterpart at almost identical BE positions. The only difference was that the peak intensities were reversed. In the PtSn/13ZA catalyst subjected to the oxidation–reduction cycle, only the components at 314.4 and 316.1 eV, the former being substantially more intense, were observed.

The surface Sn/Al, Pt/Al, and Pt/C atomic ratios derived from the XPS spectra are shown in Table 3. For the PtSn/13ZA catalyst, the causes of the deactivation lie in the formation of coke. After reaction, the Pt/C ratio had a value of 0.0018, this increasing more than 10-fold when the catalyst was regenerated (0.0210). In the PtSn/A catalyst, the deactivation also took place by coke formation and the greater ratio obtained for Pt/C (0.0060) would indicate a smaller amount of coke than in the PtSn/13ZA catalyst. The Sn/A and Pt/A ratios did not change with regeneration treatment.

DISCUSSION

Microstructural study by HREM of PtSn/A and PtSn/ZA systems clearly indicates the complexity of the bimetallic phases. This observation provides a solid argument to preclude the use of H_2 chemisorption measurements to calculate metal dispersion. Contradictory results have been reported in literature concerning the effect of tin on H_2 uptake in PtSn/A systems. In some cases, hydrogen uptakes have been used to calculate the dispersion of Pt in PtSn/A catalysts, dispersion being defined by the H_{sur}/Pt_{tot} ratio. We believe, however, that this can only be a very rough approach because tin modifies the chemisorption properties of exposed Pt atoms either by changing the chemisorption stoichiometry of the H adsorbate on Pt, or by forming a PtSn alloy, which could chemisorb H_2 in a different manner from pure Pt. Accordingly, in this case no attempt was made to calculate the turnover frequencies (TOF) in the ODH reaction.

From the BE of Sn $3d_{5/2}$ peak it is difficult to discriminate between Sn^{II} oxide and Sn^{IV} oxide (23, 24) owing to the close proximity of the BE of the core electrons of Sn in the two oxides. However, the high resolution Sn $3d_{5/2}$ spectra of the used PtSn/A and PtSn/13ZA catalysts (Figs. 13 and 14, respectively) indicate that a major fraction of tin oxide, characterized by a BE at 487.8 eV, is in the highest oxidation state (Sn^{IV}), with only a minor proportion of Sn^{II} (BE component at 486.8 eV). The absence of any other component at a BE of around 485 eV precludes the formation of metallic tin. Thus, it appears that—under the conditions of the ODH of complete O_2 consumption—the surface tin atoms are oxidized to SnO and SnO_2. However, the oxidation state of tin changes drastically if the catalysts are subjected to an *in situ* reoxidation–reduction cycle. In this case, the observation of an Sn $3d_{5/2}$ component at 485.3 eV points to the formation of an important proportion of tin as Sn^0 or alloyed with Pt, which is consistent with many other previous reports (12, 15, 25–29). According to Sexton *et al.* (30), XPS would be able to identify Sn^0 in the interior of PtSn alloy particles provided that 5% or more of the total tin present in the surface layers were in the zero-valent state. According to Adkins and Davis (31), if Sn^0 were present to an extent of 15% or more of the amount of $Sn^{II,IV}$, XPS would be able to detect it. As pointed out by Burch (32), although tin is to a large extent reduced to Sn^{II} on an Al_2O_3 support and this Sn^{II} is anchored on the support, it could influence the properties of Pt particles close to the tin. Small amounts of Sn^0 in the form of an alloy or solid solution with Pt could exert quite a large effect on performance because 15 at% tin is sufficient to fill the holes in the Pt 5d band.

As seen with photoelectron spectroscopy, one dominant feature of the used catalysts is the deposition of carbon on the catalyst surface. Thermodynamic calculations predict carbon formation, and heavy coking has been reported under oxidative (33) and steam cracking (34) reaction conditions. There are two possible secondary reactions responsible for carbon deposition, including olefin cracking and CO disproportionation. However, not all the secondary reactions necessarily involve significant carbon deposition. This is because once C_4 olefins have been formed they can crack to smaller olefins. Of particular interest is the smaller methylene species (surface $= CH_2$ fragment) formed by these cracking reactions, which can further crack to C_s and

H_s and either combine with other H_s fragments and desorb as CH_4 or combine themselves and desorb as C_2H_4. For the catalysts subjected to an oxidation–reduction cycle, photoelectron spectroscopy revealed a much higher Pt/C atomic ratio. This is consistent with the temperature-programmed oxidation profiles of coked PtSn/K–L zeolite catalysts, in which the carbon deposit appeared to be associated with the support (35). Lin *et al*. (36) reported a similar effect upon adding tin to a Pt/Al_2O_3 catalyst. These authors observed that Sn decreased the ratio of the carbon deposited on the metal to the total carbon deposited (35). It has been suggested that Sn transports coke from surface Pt atoms to the support on PtSn/A catalysts (36–38).

The key to the better behavior of the catalysts in the ODH reaction when they have been calcined–reduced is their microstructure. By HREM it was observed that in reduced PtSn/A catalysts the small platinum particle fraction is lower than in the calcined–reduced catalysts and that the large particle fraction is particularly abundant. In our study, the oxidation–reduction treatment produced the diminution in size of Pt ensembles, which inhibits the formation of highly dehydrogenated surface species required for the competing cracking, isomerization and, coking reactions (35, 39). Lieske *et al*. (37) proposed a drag-off mechanism to explain the stabilizing effect of Sn on Pt/Al_2O_3 catalysts. According to this mechanism, the presence of Sn enlarges the average distance between Pt atoms so that the adsorbed hydrocarbon cannot readily form multiple carbon–metal bonds. Because the adsorbed *n*-butane fragments are attached less strongly to surface Pt atoms, they may be more mobile and may desorb or migrate to the support more easily.

CONCLUSIONS

(i) The microstructure of Pt and Sn particles developed on the surface of A and ZA supports was explored by HREM. The HREM images of Al_2O_3-supported catalysts revealed a trimodal particle-size distribution, with a major Pt phase exhibiting diameters in the 5- to 15-nm range with a shell of $PtSn_4$. Also, $PtSn_4$ and very large particles were detected. For the Al_2O_3–ZrO_2-supported catalysts, ZrO_2 was present as nanometer-size crystals of the tetrahedral and monoclinic phases and the metallic phases were better dispersed and more homogeneously distributed than in the PtSn/A catalysts, with smaller particles being dominant.

(ii) Surface analysis of used catalysts by XPS revealed that tin is oxidized while platinum still remains partially reduced. However, the oxidation state of tin changes drastically when the catalysts are subjected to an *in situ* reoxidation–reduction cycle. In this case, the appearance of a Sn $3d_{5/2}$ component at 485.3 eV indicates the appearance of an important proportion of tin as Sn^0 or alloyed with Pt. Another dominant feature of the used catalysts, also revealed by XPS, was carbon deposition on the catalyst surface.

(iii) The catalysts were tested in the ODH of *n*-butane under fixed experimental conditions. The catalysts subjected to calcination–reduction pretreatment exhibited better performance in the ODH reaction, and the presence of tin almost completely suppressed the isomerization reaction. Finally, the modification of the metallic Pt function by tin incorporation and simultaneously by adding ZrO_2 to the Al_2O_3 substrate resulted in an enhancement of the selectivity to 1,3-butadiene.

ACKNOWLEDGMENTS

We thank Dr. J. A. Delgado, Repsol-YPF, for insightful discussions. Support for this work was provided by Repsol-YPF. The authors are also indebted to the General Technology Management of Repsol-YPF, Madrid (Spain), for giving their permission to publish this work. C.L. thanks the CSIC (Spain) for a postdoctoral grant.

REFERENCES

1. Macleod, N., Fryer, J. R., Stirling, D., and Webb, G., *Catal. Today* **46**, 37 (1998).
2. Passos, F. B., Aranda, D. A. G., and Schmal, M., *J. Catal.* **178**, 478 (1998).
3. Golunski, S. E., and Hayes, J. W., Eur. Pat. Appl. EP 638534 A1, 1995.
4. Zaera, F., *Acc. Chem. Res.* **25**, 260 (1992).
5. Zdonik, S. B., *in* "Pyrolysis: Theory and Industrial Practice" (L. F. Albright, B. L. Crynes, and W. H. Corcoran, Eds.), p. 377. Academic Press, New York, 1983.
6. Takita, Y., Kurosaki, K., Mizuhara, Y., and Ishihara, T., *Chem. Lett.* 335 (1993).
7. Matsuda, T., Koike, I., Kubo, N., and Kikuchi, E., *Appl. Catal.* **96**, 3 (1993).
8. Huff, M., and Schmidt, L. D., *J. Catal.* **149**, 127 (1994).
9. Huff, M., and Schmidt, L. D., *J. Catal.* **155**, 82 (1995).
10. Barias, O. A., Holmen, A., and Blekkan, E. A., *J. Catal.* **158**, 1 (1996).
11. Hill, J. M., Cortright, R. D., and Dumesic, J. A., *Appl. Catal. A* **168**, 9 (1998).
12. Llorca, J., Homs, N., Leon, J., Sales, J., Fierro, J. L. G., and Ramírez de la Piscina, P., *Appl. Catal. A* **189**, 77 (1999).
13. Stagg, S. M., Querini, C. A., Alvarez, W. E., and Resasco, D. E., *J. Catal.* **168**, 75 (1997).
14. Kappenstein, C., Guerin, M., Lazar, K., Matusek, K., and Paal, Z., *J. Chem. Soc. Faraday Trans.* **94**, 2463 (1998).
15. Llorca, J., Ramirez de la Piscina, P., Fierro, J. L. G., Sales, J., and Homs, N., *J. Catal.* **156**, 139 (1995).
16. Siri, G. J., Casella, M. L., Santori, G. F., and Ferretti, O. A., *Ind. Eng. Chem. Res.* **36**, 4821 (1997).
17. Audo, C., Lambert, J. F., Che, M., and Didillon, B., *Catal. Today* **65**, 157 (2001).
18. Huang, Z., Fryer, J. R., Park, C., Stirling, D., and Webb, G., *J. Catal.* **159**, 340 (1996).
19. Llorca, J., Ramírez de la Piscina, P., Fierro, J. L. G., Sales, J., and Homs, N., *J. Mol. Catal. A* **118**, 101 (1997).
20. Srinivasan, R., Rice, L. A., and Davis, B. H., *J. Catal.* **129**, 257 (1991).
21. Larese, C., Campos-Martin, J. M., and Fierro, J. L. G., *Langmuir* **16**, 10294 (2000).
22. Wagner, C. D., Davis, L. E., Zeller, M. V., Taylor, J. A., Raymond, R. H., and Gale, L. H., *Surf. Interface Anal.* **3**, 211 (1981).
23. Lau, C. L., and Wertheim, G. K., *J. Vac. Sci. Technol.* **15**(2), 622 (1978).

24. Briggs, D., and Seah, M. P., Eds., "Practical Surface Analysis by Auger and and X-Ray Photoelectron Spectroscopy," 2nd ed. Wiley, Chichester, UK, 1990.
25. Li, Y. X., and Hsia, Y. F., *Hyperfine Interact.* **28**, 875 (1986).
26. Baronetti, G. T., de Miguel, S. R., Scelza, O. A., and Castro, A. A., *Appl. Catal.* **24**, 109 (1986).
27. Stencel, J. M., Goodman, J., and Davis, B. H., *in* "Proceedings 9th International Congress on Catalysis, Calgary, 1988" (M. J. Phillips and M. Ternan, Eds.), Vol. 3, p. 1291. The Chemical Institute of Canada, Ottawa, 1988.
28. Li, Y. X., Stencel, J. M., and Davis, B. H., *React. Kinet. Catal. Lett.* **37**(2), 273 (1988).
29. Balakrishnan, K., and Schwank, J., *J. Catal.* **127**, 287 (1991).
30. Sexton, B. A., Hughes, A. E., and Foger, K., *J. Catal.* **88**, 466 (1984).
31. Adkins, S. R., and Davis, B. H., *J. Catal.* **89**, 371 (1984).
32. Burch, R., *J. Catal.* **71**, 348 (1981).
33. Font Freide, J. J. H. M., Howard, M. J., and Lomas, T. A., EP Patent 0332289 A2, (1989) (to British Petroleum Co.).
34. Brinkmeyer, F. M., Savage, K. B., and Bridges, S. D., U.S. Patent 5,243,122 (1993) (to Phillips Petroleum, Co.).
35. Cortright, R. D., Hill, J. M., and Dumesic, J. A., *Catal. Today* **55**, 213 (2000).
36. Lin, L., Zhang, T., Zang, J., and Xu, Z., *Appl. Catal.* **67**, 11 (1990).
37. Lieske, H., Sárkány, A., and Völter, J., *Appl. Catal.* **30**, 69 (1987).
38. Barias, O. A., Holmen, A., and Blekkan, E. A., *in* "Catalyst Deactivation" (B. Delmon, and G. Froment, Eds.), p. 519. Elsevier, Amsterdam, 1994.
39. Cortright, R. D., and Dumesic, J. A., *J. Catal.* **148**, 771 (1994).